

# SCIENTIFIC REPORTS

OPEN

## Design of plasmonic Ag-TiO<sub>2</sub>/H<sub>3</sub>PW<sub>12</sub>O<sub>40</sub> composite film with enhanced sunlight photocatalytic activity towards *o*-chlorophenol degradation

Nan Lu<sup>1</sup>, Yaqi Wang<sup>1</sup>, Shiqi Ning<sup>1</sup>, Wenjing Zhao<sup>1</sup>, Min Qian<sup>2</sup>, Ying Ma<sup>1</sup>, Jia Wang<sup>1</sup>, Lingyun Fan<sup>1</sup>, Jiunan Guan<sup>1</sup> & Xing Yuan<sup>1</sup>

A series of plasmonic Ag-TiO<sub>2</sub>/H<sub>3</sub>PW<sub>12</sub>O<sub>40</sub> composite films were fabricated and immobilized by validated preparation technique. The chemical composition and phase, optical, SPR effect and pore-structure properties together with the morphology of as-prepared composite film are well-characterized. The multi-synergies of as-prepared composite films were gained by combined action of electron-capture action via H<sub>3</sub>PW<sub>12</sub>O<sub>40</sub>, visible-response induced by Ag, and Schottky-junction formed between TiO<sub>2</sub>-Ag. Under simulated sunlight, the maximal  $K_{app}$  of *o*-chlorophenol (*o*-CP) reached 0.0075 min<sup>-1</sup> which was 3.95-fold larger than that of TiO<sub>2</sub> film, while it was restrained obviously under acid condition. In the photocatalytic degradation process, ·OH and ·O<sub>2</sub><sup>-</sup> attacked preferentially *ortho* and *para* position of *o*-CP molecule, and accordingly the specific degradation pathways were speculated. The novel composite film exhibited an excellent applicability due to self-regeneration of H<sub>3</sub>PW<sub>12</sub>O<sub>40</sub>, well-protection of metal Ag<sup>0</sup> and favorable immobilization.

The increasing concerns on environment and energy crises have induced considerable researches on eliminating organic pollutants in a “green” method. Photocatalysis provides such a technique with the aid of sunlight, nevertheless, the practical application of photocatalyst, such as TiO<sub>2</sub><sup>1-3</sup>, in wastewater treatment and air pollution control is limited by its inherent drawbacks i.e. poor visible light utilization efficiency and low quantum efficiency<sup>4</sup>. Consequently, different ways of modification have been employed in which deposition of polyoxometallates (POMs) has been proved to be an excellent way to enhance the photocatalytic activity of TiO<sub>2</sub><sup>5,6</sup>. Moreover, POM can be self-generated via the redox cycle between POM and POM<sup>-</sup>, and its hexagonal cage structure can enable the reaction solution to flow through the molecules and contact with the active sites adequately. In our previous researches, a series of TiO<sub>2</sub> based photocatalysts with different textural and morphological properties have been developed via depositing 12-tungstophosphoric acid (H<sub>3</sub>PW<sub>12</sub>O<sub>40</sub>) as a kind of POM with saturation Keggin<sup>7-9</sup>. The synergism between H<sub>3</sub>PW<sub>12</sub>O<sub>40</sub> and TiO<sub>2</sub> led to an efficient electron trap effect, consequently, the electrons can rapidly transfer from the conduction band of TiO<sub>2</sub> to unoccupied W 5d orbit of POM, resulting in high degradation efficiency towards various organic pollutants including dyes (methyl orange, rhodamine B)<sup>10,11</sup>, endocrine disruptors (bisphenol A, phthalate esters)<sup>12,13</sup>. However, efficient use of visible-light is still an appealing challenge for POM-TiO<sub>2</sub> composite catalysts.

Recently, a new class of TiO<sub>2</sub> based photocatalysts have emerged via depositing plasmonic noble metal nanoparticles including silver (Ag), gold (Au), and platinum (Pt), to enhance the utilization of visible-light<sup>14-18</sup>. Compared with other photosensitizers such as organic dyes<sup>19</sup>, non-metal doping<sup>20</sup> and narrow-gap semiconductors quantum dots<sup>21</sup>, the plasmonic noble metal nanoparticles possess incomparable advantages in term of the chemical stability, flexibility, and selectivity<sup>22-25</sup>. As a result of oscillation of the free conduction band electrons,

<sup>1</sup>School of Environment, Northeast Normal University, Changchun, 130117, P.R. China. <sup>2</sup>College of Chemistry, Northeast Normal University, Changchun, 130117, P.R. China. Nan Lu and Yaqi Wang contributed equally to this work. Correspondence and requests for materials should be addressed to J.G. (email: [guanjn461@nenu.edu.cn](mailto:guanjn461@nenu.edu.cn)) or X.Y. (email: [yuanx@nenu.edu.cn](mailto:yuanx@nenu.edu.cn))

surface plasmon resonance (SPR) effect enables free carrier to transport and harvest visible light without a requirement of favorable band alignment<sup>26,27</sup>. Moreover, the Schottky barrier formed between semiconductor and noble metal significantly benefits the separation of electron-hole pairs<sup>28–30</sup>. As an especially attractive surface plasmon metal, Ag has been widely used to modify TiO<sub>2</sub> due to the properties of relatively low-cost, excellent conductivity, chemical stability, catalytic activity, and near-field enhancement<sup>31–37</sup>. Therefore, it is conceivable that introducing Ag into TiO<sub>2</sub>/H<sub>3</sub>PW<sub>12</sub>O<sub>40</sub> may enhance the visible-light catalytic activity.

Moreover, current studies on photocatalysis are mainly based on powder-type photocatalysts, which severely hinders their practical applications due to the post-treatment problems in these systems such as separation, recovery and reuse. To overcome these disadvantage, much attention has been paid to explore immobilized TiO<sub>2</sub>-based film materials<sup>38,39</sup>. Among various immobilized methods, the sol-gel method has been utilized extensively<sup>40,41</sup>. However, the occurrence of reunion and the required high temperature treatment exert a significantly adverse influence on the morphology and circulation of the immobilized materials<sup>42,43</sup>. In our previous study, a validated sol-gel-hydrothermal route followed by a spin-coating method was established, which exhibited a high catalytic stability and remarkable recyclability<sup>11,12</sup>. The hydrolysis rate was efficiently controlled by adding glacial acetic acid to avoid the reunion. Meanwhile, programmed temperature hydrothermal method with relatively low temperature was designed to ensure the crystallization of TiO<sub>2</sub> and Keggin structure of H<sub>3</sub>PW<sub>12</sub>O<sub>40</sub> in the high-pressure reactor.

Thus, a recoverable plasmonic Ag loaded TiO<sub>2</sub>/H<sub>3</sub>PW<sub>12</sub>O<sub>40</sub> composite film was designed in the current study and its photocatalytic activity was evaluated in terms of degrading *o*-chlorophenol (*o*-CP) under simulated sunlight. The morphology and structure of the composite film have been well-characterized; batch experiments were conducted to reveal the influence of Ag and H<sub>3</sub>PW<sub>12</sub>O<sub>40</sub> loading amount, initial concentration and pH value of *o*-CP on the photocatalytic performance to the target reaction; the photocatalytic mechanism and possible degradation pathways of *o*-CP were discussed deeply; finally, the recyclability of the composite films was tested by three times' *o*-CP degradation run.

## Methods

The titanium tetraisopropoxide (TTIP, 98%) was purchased from Sigma-Aldrich Corporation. H<sub>3</sub>PW<sub>12</sub>O<sub>40</sub> (GR), isopropanol (AR), AgNO<sub>3</sub> (AR), *o*-CP (AR) were purchased from China Pharmaceutical Group. Other chemicals were of reagent grade and applied without further purification. Double distilled water was utilized throughout the experimental procedures.

**Catalyst preparation.** The preparation of TiO<sub>2</sub>/H<sub>3</sub>PW<sub>12</sub>O<sub>40</sub> film is described in the previous studies<sup>11,12</sup>. On the basis, AgNO<sub>3</sub> was dropped gradually into isopropanol solution during the stirring according to certain proportion with TTIP or H<sub>3</sub>PW<sub>12</sub>O<sub>40</sub>, and the remaining steps were the same as the previous reported method. The obtained hydrogel was spin-coated onto quartz substrate (50 mm × 15 mm × 1 mm), and the as-prepared composite film was denoted as Ag(x%)-TiO<sub>2</sub>/H<sub>3</sub>PW<sub>12</sub>O<sub>40</sub>(y%), in which x and y represented the loading amount of Ag (wt%: 0.5%, 1% and 2%) and H<sub>3</sub>PW<sub>12</sub>O<sub>40</sub> (wt%: 5%, 10% and 15%), respectively. The unary TiO<sub>2</sub> and binary Ag-TiO<sub>2</sub>, TiO<sub>2</sub>/H<sub>3</sub>PW<sub>12</sub>O<sub>40</sub> films were also prepared with the above procedures.

**Catalyst characterization.** The loading amounts of Ag and H<sub>3</sub>PW<sub>12</sub>O<sub>40</sub> in the composite films were determined by a Leeman Prodigy Spec inductively coupled plasma atomic emission spectrometer. X-ray diffraction (XRD) patterns were obtained on a Rigaku D/max-3c X-ray diffractometer (Cu K $\alpha$  radiation,  $\lambda = 0.15405$  nm). UV-Vis diffuse reflectance spectra (UV-Vis/DRS) were recorded on a Cary 500 UV-Vis-NIR spectrophotometer. X-ray photoelectron spectroscopy (XPS) was performed on a VG-ADES 400 instrument with Mg K $\alpha$ -ADES source at a residual gas pressure lower than 10<sup>-8</sup> Pa. Raman scattering spectra were recorded on a Jobin-Yvon HR 800 instrument with an Ar<sup>+</sup> laser source of 488 nm wavelength in a macroscopic configuration. Field-emission scanning electron micrographs (FESEM) were obtained using a JEOL 6340 F scanning electron microscope. Nitrogen porosimetry was measured by a Micromeritics ASAP 2020. Surface areas were calculated by Brunauer-Emmett-Teller (BET) equation. Pore size distributions were calculated by BJH model based on the nitrogen desorption isotherm (samples were degassed for 1 h under vacuum at 363 K, and then for 12 h at 473 K). Transmission electron microscope (TEM) micrographs, high resolution TEM (HRTEM), and selected area electron diffraction (SAED) micrographs were recorded by a JEM-2100F HRTEM at an accelerating voltage of 200 kV.

**Photocatalytic activity test.** The photocatalytic degradation of *o*-CP was conducted in a home-made quartz photoreactor under the simulated sunlight provided by a PLS-SXE300 Xe lamp (300 W, Beijing Trustech Co. Ltd., China) placing *ca.* 15 cm above the reactor. The lamp was equipped with an IR cut filter to match the natural sunlight with the wavelength ranging from 320 to 780 nm and light intensity of 200 mW/cm<sup>2</sup> measured by a radiometer (OPHIR, Newport, USA).

In the photocatalytic system, 2 pieces of the coated films (TiO<sub>2</sub> film, Ag-TiO<sub>2</sub> film, TiO<sub>2</sub>/H<sub>3</sub>PW<sub>12</sub>O<sub>40</sub> composite film, or Ag-TiO<sub>2</sub>/H<sub>3</sub>PW<sub>12</sub>O<sub>40</sub> composite film) with a weight of *ca.* 5.0 mg were submerged in the *o*-CP solution (100 ml). Prior to irradiation, the films were maintained in dark for 30 min to reach adsorption-desorption equilibrium of *o*-CP. After irradiation, a fixed amount of *o*-CP solution was sampled and analyzed at regular intervals. The degradation degree of *o*-CP solution was analyzed by HPLC equipped with Waters 2489 UV/visible detector and symmetry C18 (4.6 × 250 mm, particle size 5  $\mu$ m), with a mobile phase of acetonitrile (40%) and H<sub>2</sub>O (60%, containing 0.1% acetic acid) at a flow rate of 0.7 ml·min<sup>-1</sup> with a detection wavelength of 254 nm. The total organic carbon (TOC) was analyzed by a TOC-500 (Shimadzu). The intermediates during *o*-CP degradation were identified by a Waters Acquity UPLC/Quattro Premier XE LC/MS system. Besides, the concentrations of low molecular weight organic acids and Cl<sup>-</sup> were tested using a DX-300 ion chromatography equipped with AS4A-SC column and CDM-II conductivity detector.

The ternary composite films with different theory loadings	H <sub>3</sub> PW <sub>12</sub> O <sub>40</sub> loading	Ag loading	P (μg·ml <sup>-1</sup> )	W (μg·ml <sup>-1</sup> )	P:W
Ag(0.5%)-TiO <sub>2</sub> /H <sub>3</sub> PW <sub>12</sub> O <sub>40</sub> (10%)	7.47%	0.23%	3.687	44.321	12.021
Ag(1%)-TiO <sub>2</sub> /H <sub>3</sub> PW <sub>12</sub> O <sub>40</sub> (10%)	7.43%	0.45%	3.621	43.502	12.014
Ag(2%)-TiO <sub>2</sub> /H <sub>3</sub> PW <sub>12</sub> O <sub>40</sub> (10%)	7.40%	1.27%	3.598	43.216	12.011
Ag(1%)-TiO <sub>2</sub> /H <sub>3</sub> PW <sub>12</sub> O <sub>40</sub> (5%)	3.32%	0.50%	1.478	17.720	11.989
Ag(1%)-TiO <sub>2</sub> /H <sub>3</sub> PW <sub>12</sub> O <sub>40</sub> (15%)	12.46%	0.40%	7.985	95.788	11.996

**Table 1.** Actual loadings of H<sub>3</sub>PW<sub>12</sub>O<sub>40</sub> and Ag in composite film.

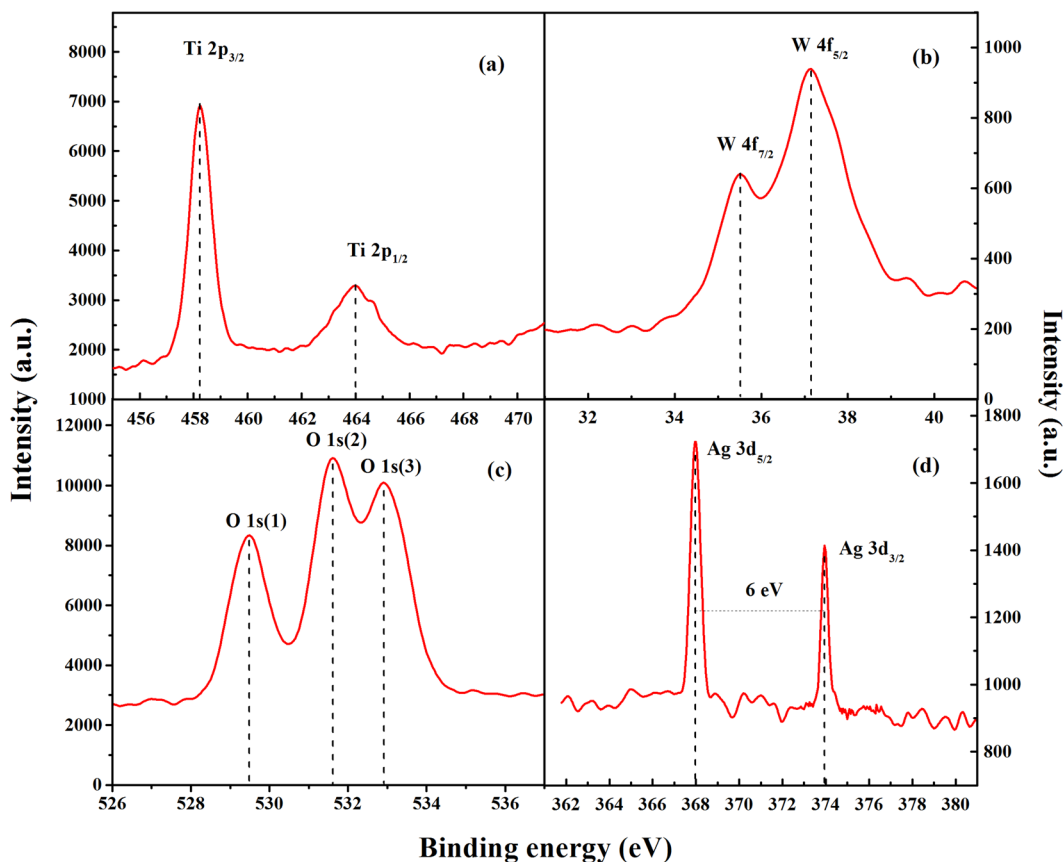


**Figure 1.** XPS survey spectra of the Ag-TiO<sub>2</sub>/H<sub>3</sub>PW<sub>12</sub>O<sub>40</sub> film in the Ti 2p (a), W 4f (b), O 1s (c), and Ag 3d (d) binding energy regions.

## Results and Discussion

**Characterization of the catalysts.** *ICP-AES and XPS.* The composition and structure of Ag-TiO<sub>2</sub>/H<sub>3</sub>PW<sub>12</sub>O<sub>40</sub> composite films were informed by ICP-AES (Table 1) and XPS (Fig. 1), respectively. The loadings of H<sub>3</sub>PW<sub>12</sub>O<sub>40</sub> and Ag in a serial of Ag-TiO<sub>2</sub>/H<sub>3</sub>PW<sub>12</sub>O<sub>40</sub> composite films are listed in Table 1. The results indicated that Keggin unit and metallic Ag were successfully loaded by the current methods and the saturation Keggin structure of H<sub>3</sub>PW<sub>12</sub>O<sub>40</sub> was retained integrally in the composite film with a P: W ratio of 1:12. Figure 1 shows that XPS spin-orbit lines of Ti 2p<sub>3/2</sub> (458.3 eV), Ti 2p<sub>1/2</sub> (464.0 eV), W 4f<sub>7/2</sub> (35.5 eV), W 4f<sub>5/2</sub> (37.2 eV), Ag 3d<sub>5/2</sub> (368.0 eV) and Ag 3d<sub>3/2</sub> (374.0 eV) were characteristic of Ti(IV) oxidation state, W(IV) oxidation state and metallic Ag in Ag-TiO<sub>2</sub>/H<sub>3</sub>PW<sub>12</sub>O<sub>40</sub> composite film, respectively<sup>29–31</sup>. O 1s XPS line of Ag-TiO<sub>2</sub>/H<sub>3</sub>PW<sub>12</sub>O<sub>40</sub> composite film exhibited three peaks at 529.5 eV, 531.6 eV and 532.9 eV, originating from lattice oxygen species of TiO<sub>2</sub>, Keggin unit and adsorbed oxygen, respectively<sup>44,45</sup>. Thus, it can be concluded that (1) according to the location of Ti 2p<sub>3/2</sub> and Ti 2p<sub>1/2</sub>, TiO<sub>2</sub> was in anatase phase in Ag-TiO<sub>2</sub>/H<sub>3</sub>PW<sub>12</sub>O<sub>40</sub> composite film<sup>46</sup>; (2) compared with pure TiO<sub>2</sub> and H<sub>3</sub>PW<sub>12</sub>O<sub>40</sub>, both Ti 2p and W 4f XPS lines of Ag-TiO<sub>2</sub>/H<sub>3</sub>PW<sub>12</sub>O<sub>40</sub> composite film shifted toward low values, implying the formation of (≡Ti-OH)<sub>n</sub><sup>+</sup>[H<sub>3-n</sub>PW<sub>12</sub>O<sub>40</sub>]<sup>n</sup> between Keggin unit and TiO<sub>2</sub> support via Ti-O-W bond<sup>12</sup>; (3) the introduction of metallic Ag was confirmed by a spin energy separation of 6.0 eV<sup>47</sup>, since under heating parent AgNO<sub>3</sub> was decomposed gradually into metallic Ag that tended to aggregate to form nano-crystals, as the following reactions<sup>48</sup>:

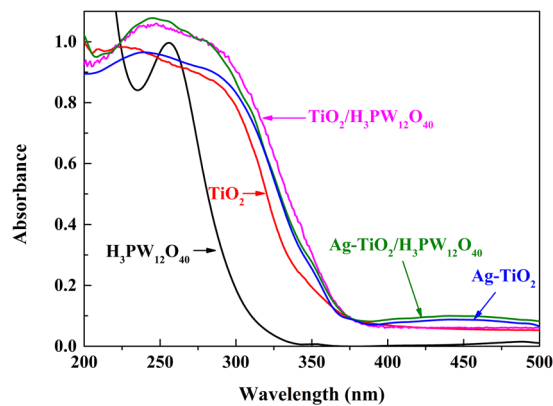


**Figure 2.** UV-Vis DRS of TiO<sub>2</sub>, H<sub>3</sub>PW<sub>12</sub>O<sub>40</sub>, Ag-TiO<sub>2</sub>, TiO<sub>2</sub>/H<sub>3</sub>PW<sub>12</sub>O<sub>40</sub> and Ag-TiO<sub>2</sub>/H<sub>3</sub>PW<sub>12</sub>O<sub>40</sub> film.

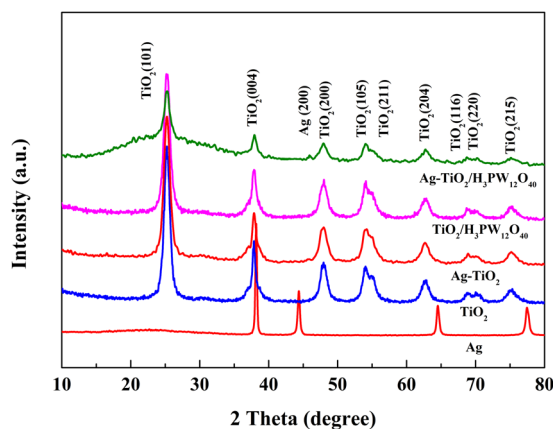


**Figure 3.** XRD patterns of TiO<sub>2</sub>, Ag, Ag-TiO<sub>2</sub>, TiO<sub>2</sub>/H<sub>3</sub>PW<sub>12</sub>O<sub>40</sub> and Ag-TiO<sub>2</sub>/H<sub>3</sub>PW<sub>12</sub>O<sub>40</sub> film.



**UV-Vis DRS.** UV-Vis DRS analysis of TiO<sub>2</sub>, H<sub>3</sub>PW<sub>12</sub>O<sub>40</sub>, Ag-TiO<sub>2</sub>, TiO<sub>2</sub>/H<sub>3</sub>PW<sub>12</sub>O<sub>40</sub> and Ag-TiO<sub>2</sub>/H<sub>3</sub>PW<sub>12</sub>O<sub>40</sub> is illustrated in Fig. 2. Compared with TiO<sub>2</sub> film, a broad and strong absorption was exhibited from 200 to 400 nm, which was contributed to the characteristic absorption peak of H<sub>3</sub>PW<sub>12</sub>O<sub>40</sub>; meanwhile a significant redshift of TiO<sub>2</sub>/H<sub>3</sub>PW<sub>12</sub>O<sub>40</sub> film was observed, which was derived from the generation of narrow band gap through the hybridization of Ti 3d and W 5d orbit in TiO<sub>2</sub>/H<sub>3</sub>PW<sub>12</sub>O<sub>40</sub> film<sup>12</sup>. It is worth noting that owing to SPR effect of metallic Ag<sup>49</sup>, both Ag-TiO<sub>2</sub> and Ag-TiO<sub>2</sub>/H<sub>3</sub>PW<sub>12</sub>O<sub>40</sub> composite film showed a light response in visible-light region (400–500 nm), which was superior to other modification methods<sup>50,51</sup>. Overall, the introduction of Ag extended the light response region and increased the light harvesting efficiency.

**XRD and TEM.** Figure 3 presents XRD patterns of TiO<sub>2</sub>, Ag, Ag-TiO<sub>2</sub>, TiO<sub>2</sub>/H<sub>3</sub>PW<sub>12</sub>O<sub>40</sub> and Ag-TiO<sub>2</sub>/H<sub>3</sub>PW<sub>12</sub>O<sub>40</sub>. The results indicated that all films showed well-indexed anatase phase of TiO<sub>2</sub> (JCPDS 21–1272)<sup>52</sup>. The peaks at 38.1°, 44.3°, 64.4°, and 77.4° can be indexed to (111), (200), (220), and (311) diffractions of cubic structured Ag (JCPDS 65–2871), respectively<sup>44</sup>. It exhibited that Ag was loaded in cubic phase with the weak diffraction at 46.5° in both as-prepared Ag-TiO<sub>2</sub> and Ag-TiO<sub>2</sub>/H<sub>3</sub>PW<sub>12</sub>O<sub>40</sub> film. Meanwhile, compared with pure TiO<sub>2</sub>, the crystallinity of Ag-TiO<sub>2</sub>/H<sub>3</sub>PW<sub>12</sub>O<sub>40</sub> composite film decreased, owing to the fine dispersion of Ag nanoparticles throughout the anatase lattice, which restricted the growth of crystallite.

Ag<sup>0</sup> nanoparticles were well dispersed as the dark dots in TEM image (Fig. 4) and incorporated into Ag-TiO<sub>2</sub>/H<sub>3</sub>PW<sub>12</sub>O<sub>40</sub> film. HRTEM image (Fig. 5) revealed a clear interface combination between the continuity of lattice fringes of TiO<sub>2</sub> and metallic Ag nanoparticles indicating the formation of the heterojunction. At the interface,

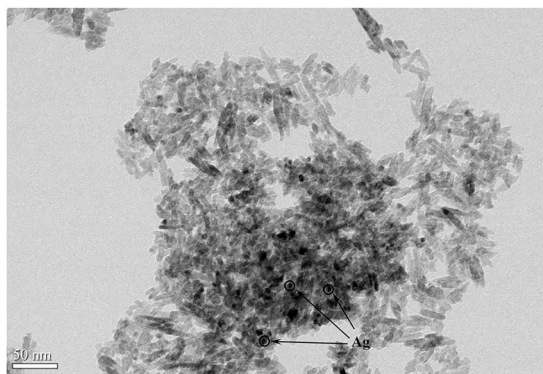


**Figure 4.** TEM image of Ag-TiO<sub>2</sub>/H<sub>3</sub>PW<sub>12</sub>O<sub>40</sub> film.

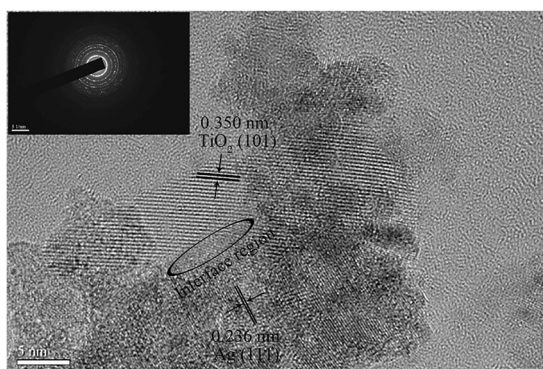


**Figure 5.** HRTEM image of Ag-TiO<sub>2</sub>/H<sub>3</sub>PW<sub>12</sub>O<sub>40</sub> film (Inset: SEAD pattern).

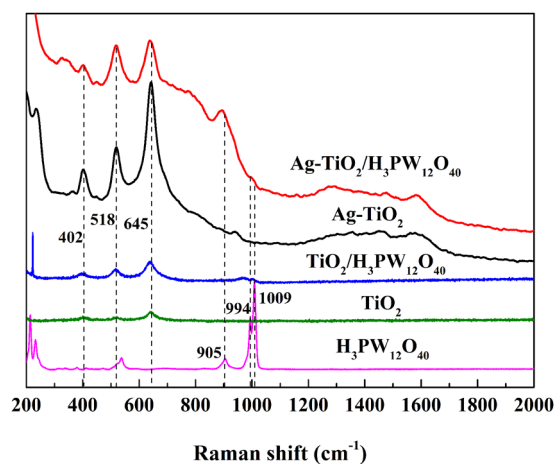


**Figure 6.** Raman spectra of H<sub>3</sub>PW<sub>12</sub>O<sub>40</sub>, TiO<sub>2</sub>, TiO<sub>2</sub>/H<sub>3</sub>PW<sub>12</sub>O<sub>40</sub>, Ag-TiO<sub>2</sub> and Ag-TiO<sub>2</sub>/H<sub>3</sub>PW<sub>12</sub>O<sub>40</sub> film.

electrons flow from one material with the high-energy Fermi level to another with the low-energy Fermi level. Whereas, the Schottky barrier that formed at the heterojunction acted as an electron sink resulting in a depletion layer that maintained the charge separation<sup>53–55</sup>.

Both anatase TiO<sub>2</sub> and cubic Ag crystallites were reconfirmed in the as-prepared Ag-TiO<sub>2</sub>/H<sub>3</sub>PW<sub>12</sub>O<sub>40</sub> corresponding to the characteristic lattice fringe of 0.35 nm (101) and 0.236 nm (111), respectively. Furthermore, in SAED pattern of Ag-TiO<sub>2</sub>/H<sub>3</sub>PW<sub>12</sub>O<sub>40</sub> film (inset of Fig. 5), a set of concentric rings corresponded to (101), (004), (200), (211), and (204) diffraction of anatase phase from the inner to the outer.

**Raman.** The Raman spectra of H<sub>3</sub>PW<sub>12</sub>O<sub>40</sub>, TiO<sub>2</sub>, TiO<sub>2</sub>/H<sub>3</sub>PW<sub>12</sub>O<sub>40</sub>, Ag-TiO<sub>2</sub> and Ag-TiO<sub>2</sub>/H<sub>3</sub>PW<sub>12</sub>O<sub>40</sub> film were presented in Fig. 6. The peaks at 402 cm<sup>-1</sup> (*B<sub>1g</sub>*), 518 cm<sup>-1</sup> (*B<sub>1g</sub>*) and 645 cm<sup>-1</sup> (*E<sub>g</sub>*) originated from anatase

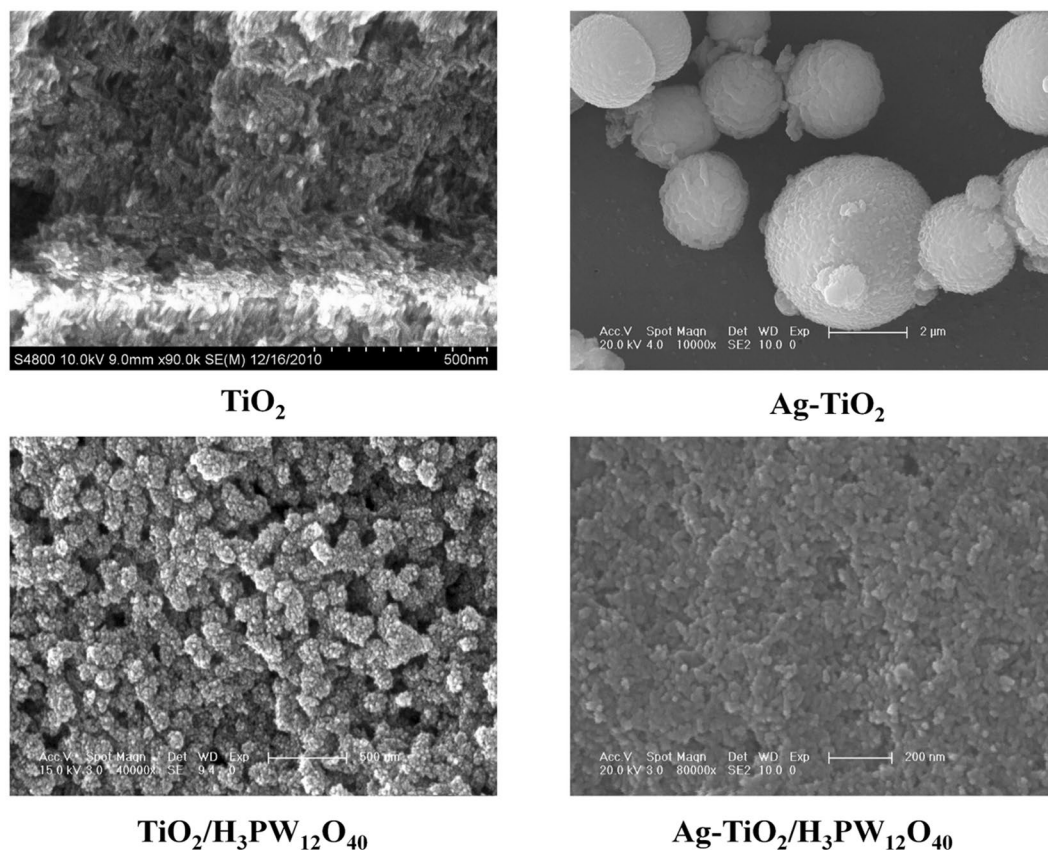


**Figure 7.** FESEM of  $\text{TiO}_2$ ,  $\text{Ag-TiO}_2$ ,  $\text{TiO}_2/\text{H}_3\text{PW}_{12}\text{O}_{40}$ , and  $\text{Ag-TiO}_2/\text{H}_3\text{PW}_{12}\text{O}_{40}$  film.

$\text{TiO}_2$ , and those at  $905\text{ cm}^{-1}$ ,  $994\text{ cm}^{-1}$ , and  $1009\text{ cm}^{-1}$  corresponded to stretching vibrations of W-O-W bonds, W=O bonds of Keggin unit and P-O bonds of  $\text{PO}_4$  units.

The surface-enhanced Raman scattering (SERS) signals indicated a strong SPR effect was generated in all the Ag-deposited films in spite of such a low Ag deposition amount. Compared with no Ag-deposited film, SPR excited by visible light would lead to an enhanced electromagnetic field around the nanoparticle, which could significantly promote the generation of “hot electron” at the interface of metal particle Ag and semiconductor  $\text{TiO}_2$ . Furthermore, a potential energy difference ( $E_{\text{SPR}} - \varphi_b$ ) between potential energy ( $E_{\text{SPR}}$ ) and Schottky barrier ( $\varphi_b$ ) was also established at the interface according to the energy band structure feature of Ag and  $\text{TiO}_2$  crystal, which could facilitate the transfer of “hot electrons” from Ag to the conduction band (CB) of  $\text{TiO}_2$  and hinder the reverse transfer at the same time. While the shift of Raman peaks may be owing to the alterations of electronic density induced by electrons transfer among  $\text{TiO}_2$ ,  $\text{H}_3\text{PW}_{12}\text{O}_{40}$  and Ag, which may improve the activity of catalyst. It was also agreed with other reports<sup>56,57</sup>.

**SEM.** As shown by FESEM (Fig. 7), the as-prepared  $\text{TiO}_2$ ,  $\text{Ag-TiO}_2$ ,  $\text{TiO}_2/\text{H}_3\text{PW}_{12}\text{O}_{40}$ , and  $\text{Ag-TiO}_2/\text{H}_3\text{PW}_{12}\text{O}_{40}$  film varied considerably in morphology.  $\text{TiO}_2$  particles illustrated a regular rice shape with a size of ca. 80 nm;  $\text{Ag-TiO}_2$  particles were composed with spheres of  $\text{TiO}_2$  (2–4  $\mu\text{m}$ ) and Ag (ca. 500 nm);  $\text{TiO}_2/\text{H}_3\text{PW}_{12}\text{O}_{40}$  particles displayed as spheres with diameters ranging between 80–100 nm covered by packed humps; whereas the surface of  $\text{Ag-TiO}_2/\text{H}_3\text{PW}_{12}\text{O}_{40}$  particles became smoother than that of  $\text{TiO}_2/\text{H}_3\text{PW}_{12}\text{O}_{40}$  due to the deposition of Ag into the pore structures of  $\text{TiO}_2/\text{H}_3\text{PW}_{12}\text{O}_{40}$ . Ti, P, W, and Ag were observed to distribute homogeneously in  $\text{Ag-TiO}_2/\text{H}_3\text{PW}_{12}\text{O}_{40}$  film by EDS analysis (Fig. 8).

**BET and BJH.** Figure 9 exhibits the adsorbed nitrogen amounts increased rapidly at  $p/p_0 < 0.1$  and H3 hysteresis loop excited at  $p/p_0 = 0.4\text{--}0.8$ , indicating the presence of microporosity (<2 nm) and mesoporosity (2–50 nm) in the prepared photocatalysts ( $\text{TiO}_2$ ,  $\text{Ag-TiO}_2$ ,  $\text{TiO}_2/\text{H}_3\text{PW}_{12}\text{O}_{40}$  and  $\text{Ag-TiO}_2/\text{H}_3\text{PW}_{12}\text{O}_{40}$ ). BET surface area and pore volume of each prepared photocatalyst are summarized in Table 2. These results were consistent with BJH desorption pore distribution curves and pore diameters calculated by BJH method (Fig. 10). BET surface area ( $169.9\text{ m}^2\text{g}^{-1}$ ) and pore volume ( $0.4390\text{ cm}^3\text{g}^{-1}$ ) of  $\text{TiO}_2/\text{H}_3\text{PW}_{12}\text{O}_{40}$  was higher than those of  $\text{TiO}_2$  ( $158.6\text{ m}^2\text{g}^{-1}$ ;  $0.4240\text{ cm}^3\text{g}^{-1}$ ) due to the formation of  $\text{TiO}_2/\text{H}_3\text{PW}_{12}\text{O}_{40}$  framework via Ti-O-W bonds. Whereas, after depositing of Ag, BET surface area and pore volume decreased to  $159.1\text{ m}^2\text{g}^{-1}$  and  $0.4256\text{ cm}^3\text{g}^{-1}$ , respectively. It can be concluded that Ag may be inserted into the pore structures of  $\text{TiO}_2/\text{H}_3\text{PW}_{12}\text{O}_{40}$ , which enhanced the stability of metallic Ag<sup>32</sup>. In spite of this, BET surface area of  $\text{Ag-TiO}_2/\text{H}_3\text{PW}_{12}\text{O}_{40}$  was much higher than that of commercial  $\text{TiO}_2\text{ P25}$  ( $50\text{ m}^2\text{g}^{-1}$ ).

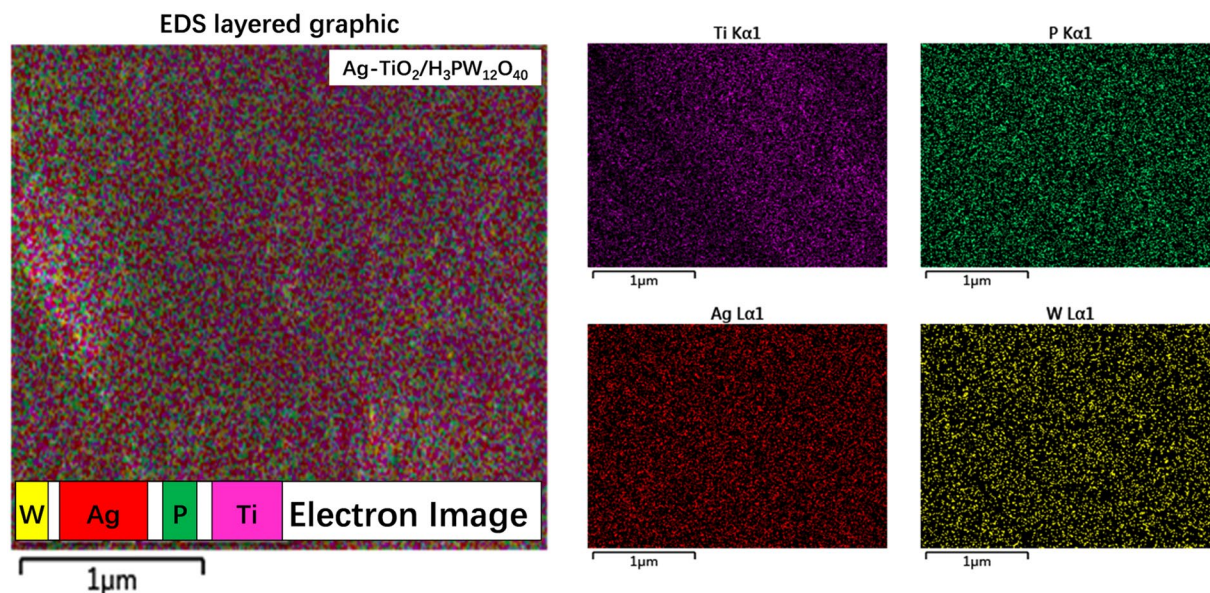


**Figure 8.** EDS mapping of  $\text{TiO}_2$ ,  $\text{Ag-TiO}_2$ ,  $\text{TiO}_2/\text{H}_3\text{PW}_{12}\text{O}_{40}$ , and  $\text{Ag-TiO}_2/\text{H}_3\text{PW}_{12}\text{O}_{40}$  film (Ti: Violet, P: Green, Ag: Red, and W: Yellow).

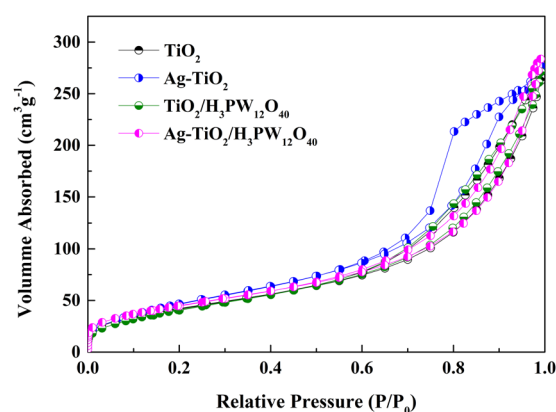


**Figure 9.** Nitrogen adsorption-desorption isotherms of  $\text{TiO}_2$ ,  $\text{Ag-TiO}_2$ ,  $\text{TiO}_2/\text{H}_3\text{PW}_{12}\text{O}_{40}$  and  $\text{Ag-TiO}_2/\text{H}_3\text{PW}_{12}\text{O}_{40}$ .

Sample	$S_{\text{BET}}$ ( $\text{m}^2\cdot\text{g}^{-1}$ )	$V_p$ ( $\text{cm}^3\cdot\text{g}^{-1}$ )
$\text{TiO}_2$	158.6	0.4240
$\text{Ag-TiO}_2$	182.2	0.4985
$\text{TiO}_2/\text{H}_3\text{PW}_{12}\text{O}_{40}$	169.9	0.4390
$\text{Ag-TiO}_2/\text{H}_3\text{PW}_{12}\text{O}_{40}$	159.1	0.4256
Commercial $\text{TiO}_2$ P25	50	—

**Table 2.** The BET surface area and pore volume of the catalysts.

**Photocatalytic test.** As a kind of persistent organic pollutant and priority pollutant listed by US EPA, o-CP was employed to evaluate the photocatalytic activity of as-prepared  $\text{Ag-TiO}_2/\text{H}_3\text{PW}_{12}\text{O}_{40}$  composite film under the simulated sunlight, together with  $\text{TiO}_2$ ,  $\text{Ag-TiO}_2$  and  $\text{TiO}_2/\text{H}_3\text{PW}_{12}\text{O}_{40}$  as comparisons. Moreover, the influencing factors were also investigated including the loading amounts of  $\text{H}_3\text{PW}_{12}\text{O}_{40}$  and Ag, initial o-CP concentration, initial pH value as well as the kinetics of o-CP photodegradation.

**Comparison of photocatalytic activity among  $\text{TiO}_2$ ,  $\text{Ag-TiO}_2$ ,  $\text{TiO}_2/\text{H}_3\text{PW}_{12}\text{O}_{40}$  and  $\text{Ag-TiO}_2/\text{H}_3\text{PW}_{12}\text{O}_{40}$ .** Figure 11 illustrates the photocatalytic degradation of o-CP ( $5\text{ mg}\cdot\text{L}^{-1}$ , 100 ml, pH = 6.3)

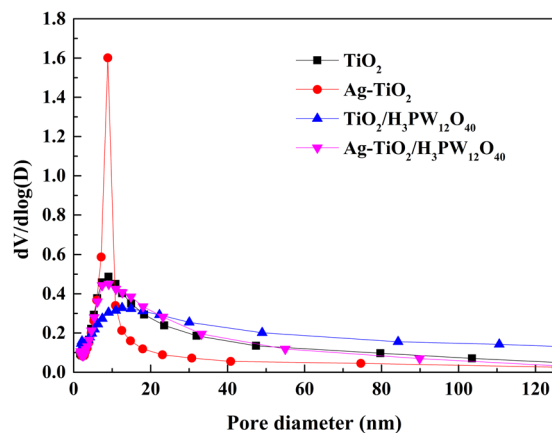


**Figure 10.** Pore size distribution profiles of  $\text{TiO}_2$ ,  $\text{Ag-TiO}_2$ ,  $\text{TiO}_2/\text{H}_3\text{PW}_{12}\text{O}_{40}$  and  $\text{Ag-TiO}_2/\text{H}_3\text{PW}_{12}\text{O}_{40}$ .

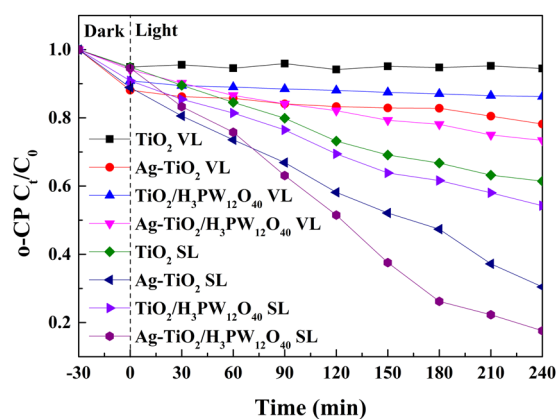


**Figure 11.** The photocatalytic activity of  $\text{TiO}_2$ ,  $\text{Ag-TiO}_2$ ,  $\text{TiO}_2/\text{H}_3\text{PW}_{12}\text{O}_{40}$  and  $\text{Ag-TiO}_2/\text{H}_3\text{PW}_{12}\text{O}_{40}$  towards o-CP degradation. (VL: Visible light; SL: Simulated sunlight).

by different catalysts under simulated sunlight irradiation. After 4 h irradiation, the degradation efficiency of o-CP was 82.40% by  $\text{Ag-TiO}_2/\text{H}_3\text{PW}_{12}\text{O}_{40}$  composite film, 69.55% by  $\text{Ag-TiO}_2$  composite film, 45.75% by  $\text{TiO}_2/\text{H}_3\text{PW}_{12}\text{O}_{40}$  composite film, and 38.55% by  $\text{TiO}_2$  film.  $\text{H}_3\text{PW}_{12}\text{O}_{40}$  improved the photocatalytic activity of  $\text{TiO}_2$ , owing to the synergistic effects between Keggin unit and  $\text{TiO}_2$ , which hindered the recombination of  $h^+e^-$  pairs efficiently<sup>12,13</sup>. Additionally, loading of Ag could not only enhance the quantum efficiency via generating Schottky junction at the interface between Ag and  $\text{TiO}_2$  (Fig. 5), but also increase the absorption of visible-light due to SPR effect, which has been confirmed by the above characterization (Fig. 2).

In order to clarify the enhancement of SPR effect, o-CP photocatalytic degradation was carried out under visible light (The lamp was equipped with the filter to cut UV light with 200–400 nm wavelength). After introducing Ag into  $\text{TiO}_2$  and  $\text{TiO}_2/\text{H}_3\text{PW}_{12}\text{O}_{40}$  film, the degradation efficiency towards o-CP increased from 5.55% ( $\text{TiO}_2$ ) to 21.80% ( $\text{Ag-TiO}_2$ ), and from 13.75% ( $\text{TiO}_2/\text{H}_3\text{PW}_{12}\text{O}_{40}$ ) to 26.60% ( $\text{Ag-TiO}_2/\text{H}_3\text{PW}_{12}\text{O}_{40}$ ) (Fig. 11), which was attributed to the loading of plasmonic metal.

The adsorption capacity of all the photocatalysts (Fig. S1 of Supporting Information) was limited ( $\text{TiO}_2$ : 6.67%;  $\text{Ag-TiO}_2$ : 12.38%;  $\text{TiO}_2/\text{H}_3\text{PW}_{12}\text{O}_{40}$ : 9.94%;  $\text{Ag-TiO}_2/\text{H}_3\text{PW}_{12}\text{O}_{40}$ : 5.89%) even though they possessed large BET surface area, which could be attributed to the low amount of the catalyst (ca. 5.0 mg) in the current system. Compared with other related researches, the as-prepared  $\text{Ag-TiO}_2/\text{H}_3\text{PW}_{12}\text{O}_{40}$  composite film represented a more excellent property on the light utilization with a comparable catalyst amount<sup>58</sup>.

**Effect of  $\text{H}_3\text{PW}_{12}\text{O}_{40}$  loading amount.** The adsorption of o-CP ( $5 \text{ mg}\cdot\text{L}^{-1}$ , 100 ml, pH = 6.3) on  $\text{Ag}(1\%)\text{-TiO}_2/\text{H}_3\text{PW}_{12}\text{O}_{40}$  with different  $\text{H}_3\text{PW}_{12}\text{O}_{40}$  loading amount is shown in Fig. S2. The results suggested that  $\text{H}_3\text{PW}_{12}\text{O}_{40}$  loading amount did not exert a significant influence on adsorption capacity to o-CP. Figure 12 exhibits the effect of  $\text{H}_3\text{PW}_{12}\text{O}_{40}$  loading amount on the photocatalytic activity of  $\text{Ag}(1\%)\text{-TiO}_2/\text{H}_3\text{PW}_{12}\text{O}_{40}$  film. The photocatalytic activity raised obviously with the increase of  $\text{H}_3\text{PW}_{12}\text{O}_{40}$  loading amount from 5% to 10%, whereas it decreased slightly when  $\text{H}_3\text{PW}_{12}\text{O}_{40}$  loading reached 15%, since excessive amount of  $\text{H}_3\text{PW}_{12}\text{O}_{40}$  might affect light absorption<sup>11</sup>. Consequently, the degradation rate peaked at 82.40% by  $\text{Ag}(1\%)\text{-TiO}_2/\text{H}_3\text{PW}_{12}\text{O}_{40}(10\%)$ .

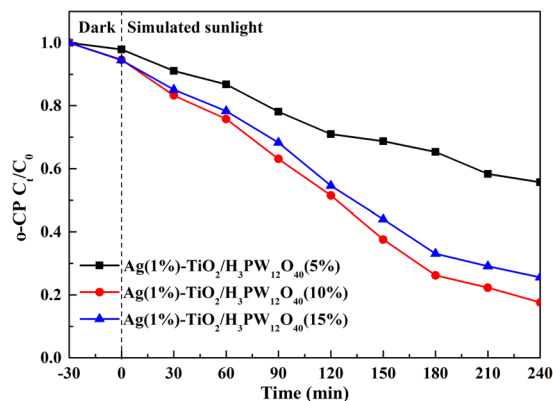


**Figure 12.** The influence of  $\text{H}_3\text{PW}_{12}\text{O}_{40}$  loading amount on the photocatalytic activity of  $\text{Ag-TiO}_2/\text{H}_3\text{PW}_{12}\text{O}_{40}$  towards o-CP degradation.

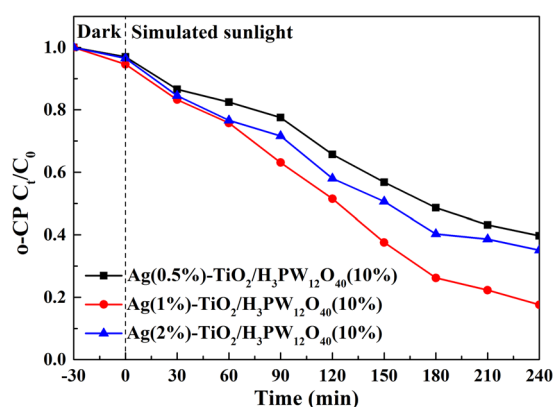


**Figure 13.** The influence of Ag loading amount on the photocatalytic activity of  $\text{Ag-TiO}_2/\text{H}_3\text{PW}_{12}\text{O}_{40}$  towards o-CP degradation.

**Effect of Ag loading amount.** Likewise, the variation of Ag loading amount in  $\text{Ag-TiO}_2/\text{H}_3\text{PW}_{12}\text{O}_{40}$  (10%) films did not alter the adsorption capability of o-CP ( $5 \text{ mg}\cdot\text{L}^{-1}$ , 100 ml,  $\text{pH} = 6.3$ ) significantly (Fig. S3). The degradation efficiency of o-CP (82.40%) peaked with a Ag loading amount of 1% in  $\text{Ag-TiO}_2/\text{H}_3\text{PW}_{12}\text{O}_{40}$  film (Fig. 13). It implied that a great majority of transferred electrons were trapped due to the strong electron accepting ability of metallic Ag, resulting in an effective separation of the electrons and holes. However, excessive Ag nanoparticle not only acted as an electron-hole recombination center, but also blocked partial UV-light that could reach the surface of  $\text{TiO}_2$ <sup>59,60</sup>, which further decreased its photocatalytic activity. Thus,  $\text{Ag}(1\%)\text{-TiO}_2/\text{H}_3\text{PW}_{12}\text{O}_{40}$  (10%) represented the maximum photoactivity, and was selected in subsequent photocatalytic experiments.

**Effect of initial concentration of o-CP.** As demonstrated in Fig. S4, the direct photolysis rate of o-CP (100 ml,  $\text{pH} = 6.3$ ) was 5.11%, 3.83% and 1.83% with initial concentrations of  $5 \text{ mg}\cdot\text{L}^{-1}$ ,  $10 \text{ mg}\cdot\text{L}^{-1}$ , and  $20 \text{ mg}\cdot\text{L}^{-1}$ , the photocatalytic degradation rate was 82.40%, 76.60% and 63.70%, respectively (Fig. 14). Thus, both the direct photolysis and photocatalytic degradation rate decreased gradually with the raise of initial concentration of o-CP by reason of the restraint on light transmittance and light utilization of catalyst. Additionally, with a fixed catalyst dosage, the more o-CP molecules adsorbed and accumulated on the film surface (Fig. S5), the less contact between the reactive oxygen species and catalyst<sup>61</sup>. Herein, the minimum initial concentration ( $5 \text{ mg}\cdot\text{L}^{-1}$ ) was the optimal condition for photocatalytic degradation.

**Effect of initial pH.** As illustrated in Fig. 15, at the alkaline conditions, the degradation rate was 79.70% at  $\text{pH} = 9.2$  and 73.80% at  $\text{pH} = 12.1$ , which was significantly higher than that at the acid condition (46.80% at  $\text{pH} = 3.1$ ). The contact of o-CP molecules with the catalyst or sunlight irradiation was intercepted under the acid condition (Figs S6 and S7), resulting in a low degradation efficiency. Under the alkaline condition, the adsorption process was hindered by the electrostatic repulsion between the electronegative composite film (both Ag and  $\text{H}_3\text{PW}_{12}\text{O}_{40}$  are fairly strong electron acceptors) and negatively charged o-CP. Whereas, the direct photodegradation rate elevated rapidly with increase of pH values, since high pH value was in favor of generation of hydroxyl ions<sup>62</sup>, which would subsequently enhance the photodegradation efficiency via forming hydroxyl radicals with holes.

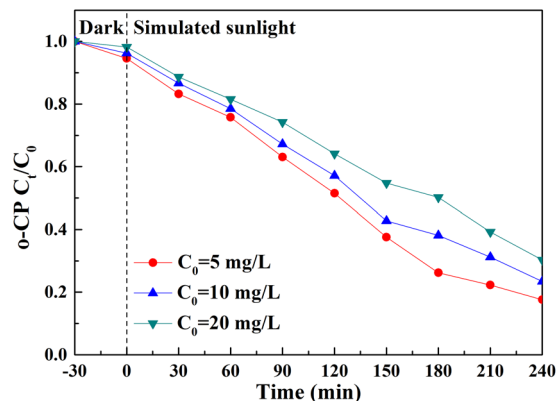


**Figure 14.** The influence of initial concentration of o-CP on the photocatalytic activity of Ag-TiO<sub>2</sub>/H<sub>3</sub>PW<sub>12</sub>O<sub>40</sub>.

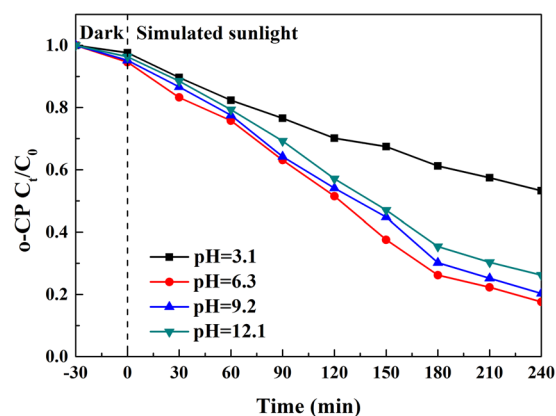


**Figure 15.** Influence of initial pH values towards o-CP degradation.

The photocatalytic degradation rate achieved the maximum value (82.40%) at pH = 6.3 due to the largest adsorption amount of o-CP. In addition, photocatalytic activity of TiO<sub>2</sub> peaked at pH<sub>pzc</sub> (pH = 6.25), which was close to the initial pH value of o-CP solution (pH = 6.3). Hence, pH = 6.3 was optimal initial pH value for the photodegradation of o-CP<sup>63,64</sup>.

**Photocatalytic kinetics.** The kinetics of photocatalytic reactions under different conditions are summarized in Table 3. The results indicated the kinetics could be well described by simplified Langmuir-Hinshelwood (L-H) Model:

$$-dc/dt = K_{app}c \quad (4)$$

in which  $K_{app}$  is the apparent constant as the basic kinetic parameter when the initial concentration is low;  $c$  is the initial concentration of the target compound.

Under the optimal condition,  $K_{app}$  of o-CP photocatalytic degradation reaction achieved 0.0075 min<sup>-1</sup> by Ag(1%)-TiO<sub>2</sub>/H<sub>3</sub>PW<sub>12</sub>O<sub>40</sub>(10%) film, which was 1.63-fold, 3.26-fold and 3.95-fold larger than that of Ag-TiO<sub>2</sub>, TiO<sub>2</sub>/H<sub>3</sub>PW<sub>12</sub>O<sub>40</sub> film and TiO<sub>2</sub> film, respectively.  $K_{app}$  fluctuated largely along with the variation of H<sub>3</sub>PW<sub>12</sub>O<sub>40</sub> loading amount and initial pH value, which suggested both of the factors exerted an essential influence on the kinetics of o-CP degradation.

**Photocatalytic Mechanism.** In general, the photocatalytic degradation can be regarded as a process of generation, transfer, and consumption of the photogenerated carriers<sup>65</sup>. The photocatalyst absorbed the incident photons with energy above the semiconductor's band gap, generating the same number of electrons and holes, in which the hole abstracted electrons from absorbed pollutants or reacted with H<sub>2</sub>O to generate ·OH; while the conduction band electrons reduced the absorbed oxygen to produce ·O<sub>2</sub><sup>-</sup> that further generated ·OH via chain reactions. In order to reveal the mechanism of enhanced photocatalytic activity of the plasmonic Ag-TiO<sub>2</sub>/H<sub>3</sub>PW<sub>12</sub>O<sub>40</sub> photocatalyst in depth, the active species generated during the process of photocatalyzed o-CP degradation were identified by free radicals and holes trapping experiments in the current study. Na<sub>2</sub>-EDTA (0.0037 g)<sup>66</sup>, isopropanol (0.1 ml)<sup>67</sup>, and benzoquinone (0.0108 g)<sup>68</sup> were employed to scavenge the holes (h<sup>+</sup>), hydroxyl radicals (·OH), and superoxide radicals (·O<sub>2</sub><sup>-</sup>), respectively. After adding Na<sub>2</sub>-EDTA, the degradation efficiency did not alter significantly, implying

Influence factor	Condition	$r_0$ (mg/L-min)	$k$ (min <sup>-1</sup> )	Kinetic equation	R
Film type	TiO <sub>2</sub>	0.0095	0.0019	$y = 0.0019x + 0.0619$	0.990
	Ag-TiO <sub>2</sub>	0.0230	0.0046	$y = 0.0046x + 0.0136$	0.990
	TiO <sub>2</sub> /H <sub>3</sub> PW <sub>12</sub> O <sub>40</sub>	0.0115	0.0023	$y = 0.0023x + 0.0782$	0.994
	Ag-TiO <sub>2</sub> /H <sub>3</sub> PW <sub>12</sub> O <sub>40</sub>	0.0377	0.0075	$y = 0.0075x - 0.1095$	0.990
H <sub>3</sub> PW <sub>12</sub> O <sub>40</sub> loading	5%	0.0122	0.0024	$y = 0.0024x + 0.0139$	0.995
	10%	0.0377	0.0075	$y = 0.0075x - 0.1095$	0.990
	15%	0.0301	0.0060	$y = 0.0060x - 0.0648$	0.992
Ag loading	0.5%	0.0199	0.0040	$y = 0.0040x - 0.0253$	0.993
	1%	0.0377	0.0075	$y = 0.0075x - 0.1095$	0.990
	2%	0.0227	0.0045	$y = 0.0045x + 0.0079$	0.993
Initial pH	3.1	0.0127	0.0025	$y = 0.0025x + 0.0278$	0.997
	6.3	0.0377	0.0075	$y = 0.0075x - 0.1095$	0.990
	9.2	0.0343	0.0069	$y = 0.0069x - 0.1077$	0.989
	12.1	0.0294	0.0059	$y = 0.0059x - 0.0815$	0.993
Initial concentration	5 mg/L	0.0377	0.0075	$y = 0.0075x - 0.1095$	0.990
	10 mg/L	0.0236	0.0047	$y = 0.0047x - 0.0677$	0.984
	20 mg/L	0.0299	0.0040	$y = 0.0060x - 0.0766$	0.992

**Table 3.** The kinetics of o-CP photocatalytic reaction.

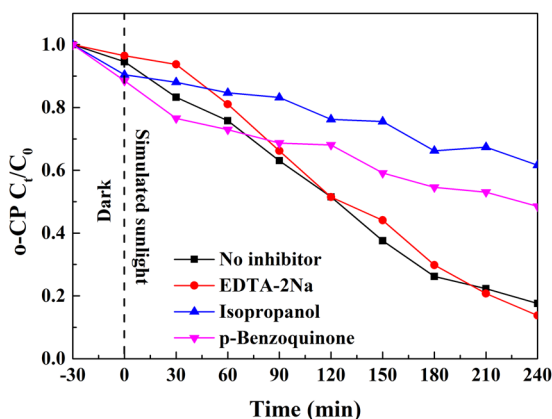


**Figure 16.** The degradation of o-CP by Ag-TiO<sub>2</sub>/H<sub>3</sub>PW<sub>12</sub>O<sub>40</sub> with different scavengers. (a) Na<sub>2</sub>-EDTA (0.0037 g); (b) isopropanol (0.1 ml); (c) benzoquinone (0.0108 g).

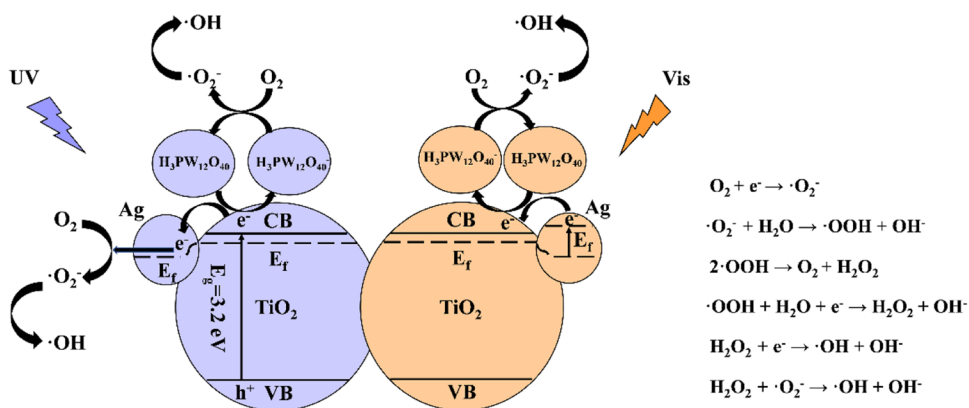


**Figure 17.** The photocatalytic mechanism of Ag-TiO<sub>2</sub>/H<sub>3</sub>PW<sub>12</sub>O<sub>40</sub> system.

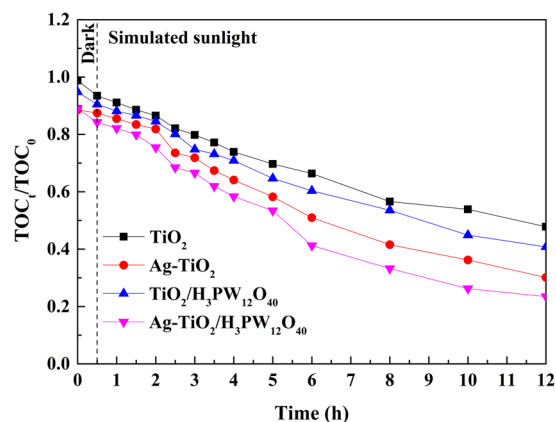


**Figure 18.** Variation of TOC during photocatalytic degradation of o-CP.

the holes played a minor role in either oxidization or generation of  $\cdot\text{OH}$  during the o-CP degradation process. Whereas, the presence of isopropanol and benzoquinone decreased the degradation rate markedly to 38.4% and 51.5%, respectively, indicating both  $\cdot\text{OH}$  and  $\cdot\text{O}_2^-$  acted as a major role during the process (Fig. 16).

The detailed photocatalytic mechanism of Ag-TiO<sub>2</sub>/H<sub>3</sub>PW<sub>12</sub>O<sub>40</sub> towards o-CP degradation under the simulated sunlight ( $320\text{ nm} < \lambda < 780\text{ nm}$ ) is illustrated in Fig. 17. Under the UV-light ( $320\text{ nm} < \lambda < 400\text{ nm}$ ), the electrons were firstly promoted from the valence band to the conduction band of TiO<sub>2</sub>, left the holes in the valence band of TiO<sub>2</sub>. Whereafter, the photogenerated electrons were transported constantly to metallic Ag and accumulated on its surface, forming the Schottky junction between Ag and TiO<sub>2</sub>. Furthermore, H<sub>3</sub>PW<sub>12</sub>O<sub>40</sub> trapped the electrons which promoted to the conduction band of TiO<sub>2</sub> generating H<sub>3</sub>PW<sub>12</sub>O<sub>40</sub><sup>-</sup>, and then self-regenerated to H<sub>3</sub>PW<sub>12</sub>O<sub>40</sub> via the redox cycling. Finally, these effectively separated electrons could be transferred to the oxygen adsorbed on the surface of Ag and H<sub>3</sub>PW<sub>12</sub>O<sub>40</sub> to generate  $\cdot\text{O}_2^-$  active groups. Under the visible light ( $400\text{ nm} < \lambda < 780\text{ nm}$ ), Ag was activated at first, the hot plasmonic electrons of Ag was subsequently transformed to the conduction band of TiO<sub>2</sub> and gathered by H<sub>3</sub>PW<sub>12</sub>O<sub>40</sub>, consequently, the generated H<sub>3</sub>PW<sub>12</sub>O<sub>40</sub><sup>-</sup> reacted with adsorbed oxygen to produce  $\cdot\text{O}_2^-$  which would further react with H<sub>2</sub>O to form  $\cdot\text{OH}$ . To sum up, both  $\cdot\text{O}_2^-$  and  $\cdot\text{OH}$  played a primary active role in the degradation of o-CP.

**Mineralization of o-CP.** The mineralization capability of Ag-TiO<sub>2</sub>/H<sub>3</sub>PW<sub>12</sub>O<sub>40</sub> film to o-CP molecules was evaluated by monitoring the variation of TOC in the reaction system during photocatalytic degradation process (Fig. 18). In order to detect it sensitively and accurately, the initial o-CP concentration was increased to 20 mg·L<sup>-1</sup>. The results indicated that in comparison with TiO<sub>2</sub>/H<sub>3</sub>PW<sub>12</sub>O<sub>40</sub> (52.20%), Ag-TiO<sub>2</sub> (69.88%) and TiO<sub>2</sub> (49.20%) film, Ag-TiO<sub>2</sub>/H<sub>3</sub>PW<sub>12</sub>O<sub>40</sub> film exhibited the highest mineralization capability, by which 76.50% of TOC was mineralized after 12 h irradiation, indicating that most of o-CP molecules as well as the organic intermediates were decomposed and mineralized.

Figure 19(a) shows that the concentrations of acetic acid and butanedioic acid peaked within 4–6 h during the degradation process, while the formic acid concentration achieved the maximum value within 4–8 h, suggesting the ring-opening reaction occurred during the o-CP degradation. The releasing rate of Cl<sup>-</sup> was low before 6 h and increased greatly after 6 h, due to the occurrence of C-Cl bond cleavage. The results implied a possibility that the ring-opening reaction of o-CP molecule mainly occurred in the early stage during the degradation process, while most of C-Cl bond were broken subsequently. At 12 h, the concentration of Cl<sup>-</sup> reached 1.58 mg·L<sup>-1</sup>, while the concentrations of low molecular weight organic acids decreased to 0.007 mg·L<sup>-1</sup>, 0.002 mg·L<sup>-1</sup> and 0.013 mg·L<sup>-1</sup> for acetic acid, butanedioic acid and formic acid, respectively, which could be further mineralized to CO<sub>2</sub> and H<sub>2</sub>O. Moreover, as shown in Fig. 19(b), the releasing of Cl<sup>-</sup> and formation of low molecular weight organic acids could decrease pH value during the process, which would impede the progress of photocatalytic degradation, as confirmed previously (Fig. 15). Therefore, the decrease of pH value during the degradation process may explain why o-CP cannot be decomposed and mineralized completely.

**Degradation pathways of o-CP.** In order to speculate the degradation pathways of o-CP in Ag-TiO<sub>2</sub>/H<sub>3</sub>PW<sub>12</sub>O<sub>40</sub> film system, the main intermediate products were detected by LC-MS (Table 4). The mass fragment peaks were identified as *o*-chlorophenol (126.8 m/z), 2-chlorohydroquinone or 3-chlorocatechol (142.8 m/z), and 2-chlorobenzoquinone (144.8 m/z). Accordingly, the possible photocatalytic degradation pathways of o-CP were as follows (Fig. 20). As the key role in the photocatalytic degradation,  $\cdot\text{OH}$  and  $\cdot\text{O}_2^-$  attacked preferentially the *ortho* and *para* position of o-CP molecule<sup>69</sup>. The *ortho* position (Path 1) was attacked by  $\cdot\text{OH}$  generating 3-chlorocatechol followed by H-abstraction, and then 5-chloropentanol was generated and further decomposed to formic acid, butanedioic acid and Cl<sup>-</sup> after ring-opening reaction; The *para* position (Path 2) was attacked by both  $\cdot\text{OH}$  and  $\cdot\text{O}_2^-$  producing 2-chlorohydroquinone and 2-chlorobenzoquinone simultaneously, hereafter, butanediol and butanedioic acid were formed via ring-opening reaction, together with chloroethylene as another intermediate product that further produced acetic acid by dechlorinating processes. Finally, o-CP can be mineralized into Cl<sup>-</sup>, CO<sub>2</sub> and H<sub>2</sub>O.

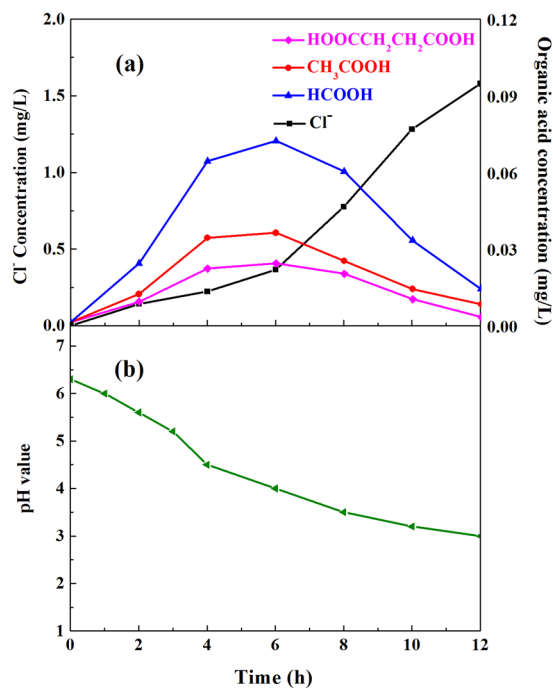


**Figure 19.** Evolution of low molecular weight organic acids and chlorine (a) and pH value (b) during photocatalytic degradation of o-CP.

	m/z	Structural formula
o-CP	126.8	
Main intermediate products	142.8	
	144.8	

**Table 4.** The chemical formulas of o-CP and the main intermediate products.

**Recyclability of the catalyst.** From viewpoint of practical applications, the recyclability is an essential aspect for the composite film photocatalyst, which can not only greatly reduce the cost but also avoid secondary pollution. In the current study, Ag(1%)-TiO<sub>2</sub>/H<sub>3</sub>PW<sub>12</sub>O<sub>40</sub>(10%) film was selected to conduct the recycling experiment under the optimum condition for three times, the composite film was dipped in ethanol to remove the absorbed o-CP molecules after each catalytic run, then washed by distilled water and dried at room temperature. The results showed that even after 3 times recycle, the composite film could still degrade more than 80.00% of o-CP (Fig. 21), and only 0.13% H<sub>3</sub>PW<sub>12</sub>O<sub>40</sub> and 0.05% Ag dropped from the film.

The electrochemical impedance spectroscopy (EIS) of TiO<sub>2</sub>, Ag-TiO<sub>2</sub>, TiO<sub>2</sub>/H<sub>3</sub>PW<sub>12</sub>O<sub>40</sub>, and Ag-TiO<sub>2</sub>/H<sub>3</sub>PW<sub>12</sub>O<sub>40</sub> film was implemented to quest their charge transport capability. It is well-known that the smaller arc radius is, the higher separation efficiency of electrons-holes becomes. As displayed in Fig. 22, arc radius of Ag-TiO<sub>2</sub>/H<sub>3</sub>PW<sub>12</sub>O<sub>40</sub> was the smallest among all the films, suggesting the least resistance for charge transfer.

The photocurrent-time (*I-t*) curves of TiO<sub>2</sub>, Ag-TiO<sub>2</sub>, TiO<sub>2</sub>/H<sub>3</sub>PW<sub>12</sub>O<sub>40</sub>, and Ag-TiO<sub>2</sub>/H<sub>3</sub>PW<sub>12</sub>O<sub>40</sub> film are shown in Fig. 23 with the cycles of light-on and light-off. Distinctly, Ag-TiO<sub>2</sub>/H<sub>3</sub>PW<sub>12</sub>O<sub>40</sub> and Ag-TiO<sub>2</sub> film represented a higher photocurrent intensity during the cycles of on-off intermittent irradiation, reconfirming that the introduction of Ag into the catalyst was feasible to increase both the quantum efficiency and separation efficiency of photogenerated electron-hole pairs, which was corresponding to the results of EIS. However, the stability of Ag-TiO<sub>2</sub> film was not the same as Ag-TiO<sub>2</sub>/H<sub>3</sub>PW<sub>12</sub>O<sub>40</sub> and its photocurrent intensity decreased after

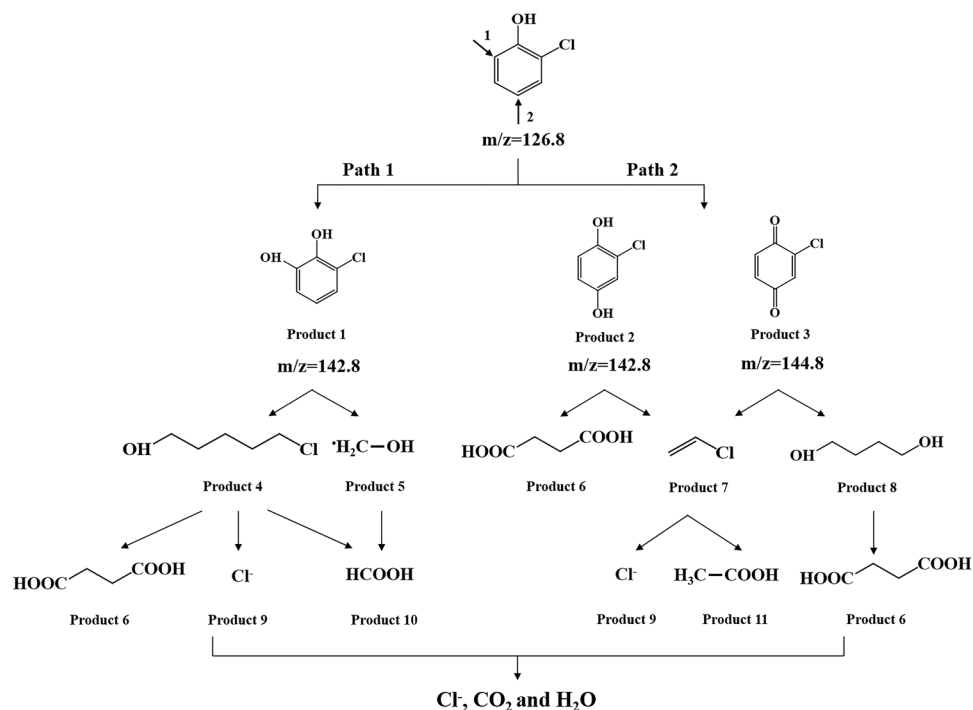


**Figure 20.** The possible photocatalytic degradation pathways of o-CP by Ag-TiO<sub>2</sub>/H<sub>3</sub>PW<sub>12</sub>O<sub>40</sub> film.

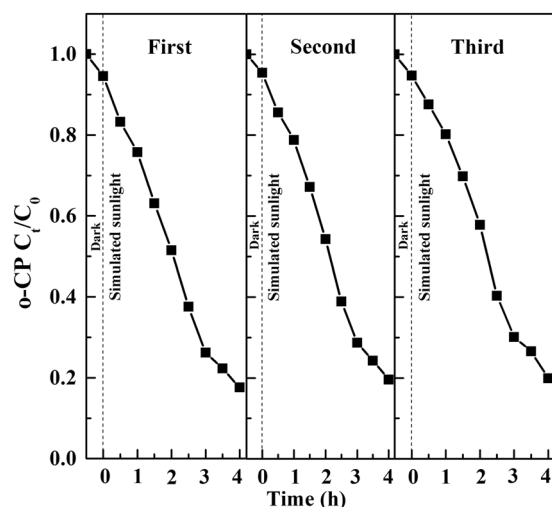


**Figure 21.** Recycling runs of Ag-TiO<sub>2</sub>/H<sub>3</sub>PW<sub>12</sub>O<sub>40</sub> film in the photocatalytic degradation of o-CP.

every cycle of light-on and light-off, which further induced the decreasing of photocatalytic activity. This can be attributed to the fact that metal Ag can be easily oxidized after depositing on the surface of TiO<sub>2</sub> particles, if the cover was absent.

Overall, an excellent photocatalytic activity, stability and reproducibility of Ag-TiO<sub>2</sub>/H<sub>3</sub>PW<sub>12</sub>O<sub>40</sub> composite film was attained from the following approaches: (1) the excellent photocatalytic activity was attributed to a large quantity of holes and electrons produced by adsorbing simulated sunlight irradiation induced by SPR effect; (2) the enhanced quantum efficiency was owing to the strong electron-accepting capability of H<sub>3</sub>PW<sub>12</sub>O<sub>40</sub> and the formation of Schottky junction via the modification with metallic Ag; (3) the excellent recyclability was due to the preferably preparation method, the self-regeneration of H<sub>3</sub>PW<sub>12</sub>O<sub>40</sub> as well as loading of Ag<sup>0</sup> into the TiO<sub>2</sub>/H<sub>3</sub>PW<sub>12</sub>O<sub>40</sub> framework.

## Conclusions

An efficient plasmonic Ag-TiO<sub>2</sub>/H<sub>3</sub>PW<sub>12</sub>O<sub>40</sub> composite film with enhanced sunlight photocatalytic activity was prepared by modified sol-gel-hydrothermal method combined with spin coating technique. It has been revealed

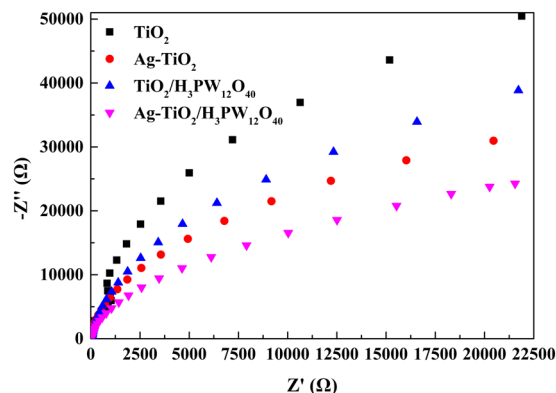


**Figure 22.** EIS Nyquist plots of  $\text{TiO}_2$ ,  $\text{Ag-TiO}_2$ ,  $\text{TiO}_2/\text{H}_3\text{PW}_{12}\text{O}_{40}$ , and  $\text{Ag-TiO}_2/\text{H}_3\text{PW}_{12}\text{O}_{40}$  film.

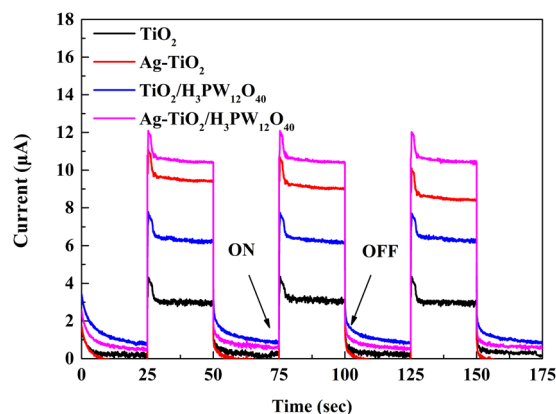


**Figure 23.** Photocurrent responses of  $\text{TiO}_2$ ,  $\text{Ag-TiO}_2$ ,  $\text{TiO}_2/\text{H}_3\text{PW}_{12}\text{O}_{40}$  and  $\text{Ag-TiO}_2/\text{H}_3\text{PW}_{12}\text{O}_{40}$  film electrodes.

that the composite film was an excellent photocatalytic activity towards o-CP degradation, mainly due to the extra active electrons and holes generated by SPR effect as well as Schottky junction via the modification with metallic Ag.  $\cdot\text{OH}$  and  $\cdot\text{O}_2^-$  were confirmed to play an essential role in photocatalytic degradation of o-CP, and the possible o-CP photodegradation pathways were put forward according to the identified intermediate products. The mineralization testified the strong oxidation ability of  $\text{Ag-TiO}_2/\text{H}_3\text{PW}_{12}\text{O}_{40}$  catalyst, which could decompose the contaminants into  $\text{CO}_2$  and  $\text{H}_2\text{O}$ . It also showed a remarkably excellent stability and recyclability of the composite film in degrading o-CP, which may greatly limit the economic cost and secondary pollution. The studies in this work provide important information on o-CP degradation, which will promote the technical development for its removal. The plasmonic composite film could be used further for the decomposition of persistent organic pollutants with low concentration in practical water and wastewater treatment.

## References

- Fujishima, A., Rao, T. N. & Tryk, D. A. Titanium dioxide photocatalysis. *J. Photochem. Photobiol. C: Photochem. Rev.* **1**, 1–21 (2000).
- Wang, F. F., Ge, W. N., Shen, T., Ye, B. J. & Fu, Z. P. The effect of bulk/surface defects ratio change on the photocatalysis of  $\text{TiO}_2$  nanosheet film. *Appl. Surf. Sci.* **410**, 513–518 (2017).
- Low, J. X., Cheng, B. C. & Yu, J. G. Surface modification and enhanced photocatalytic  $\text{CO}_2$  reduction performance of  $\text{TiO}_2$ : a review. *Appl. Surf. Sci.* **392**, 658–686 (2017).
- Gaya, U. I. & Abdullah, A. H. Heterogeneous photocatalytic degradation of organic contaminants over titanium dioxide: a review of fundamentals, progress and problems. *J. Photochem. Photobiol. C: Photochem. Rev.* **9**, 1–12 (2008).
- Jin, H., Wu, Q. & Pang, W. Photocatalytic degradation of textile dye X-3B using polyoxometalate- $\text{TiO}_2$  hybrid materials. *J. Hazard. Mater.* **141**, 123–127 (2007).
- Yang, Y., Guo, Y. H., Hu, C. W., Wang, Y. & Wang, E. Preparation of surface modifications of mesoporous titania with monosubstituted Keggin units and their catalytic performance for organochlorine pesticide and dyes under UV irradiation. *Appl. Catal., A: Gen.* **273**, 201–210 (2004).
- Li, K. X. *et al.* Design of mesostructured  $\text{H}_3\text{PW}_{12}\text{O}_{40}$ -titania materials with controllable structural orderings and pore geometries and their simulated sunlight photocatalytic activity towards diethyl phthalate degradation. *Appl. Catal. B: Environ.* **99**, 364–375 (2010).
- Li, L., Wu, Q., Guo, Y. H. & Hu, C. W. Nanosize and bimodal porous polyoxotungstate-anatase  $\text{TiO}_2$  composites: preparation and photocatalytic degradation of organophosphorus pesticide using visible-light excitation. *Micropor. Mesopor. Mat.* **87**, 1–9 (2005).
- Li, J. H. *et al.* Mesoporous titania-based  $\text{H}_3\text{PW}_{12}\text{O}_{40}$  composite by a block copolymer surfactant-assisted templating route: preparation, characterization, and heterogeneous photocatalytic properties. *Desalination* **255**, 107–116 (2010).

10. Li, K. X. *et al.* Design of ordered mesoporous  $\text{H}_3\text{PW}_{12}\text{O}_{40}$ -titania materials and their photocatalytic activity to dye methyl orange degradation. *Catal. Commun.* **11**, 839–843 (2010).
11. Lu, N. *et al.* Design of polyoxometallate-titania composite film ( $\text{H}_3\text{PW}_{12}\text{O}_{40}/\text{TiO}_2$ ) for the degradation of an aqueous dye Rhodamine B under the simulated sunlight irradiation. *J. Hazard. Mater.* **199–200**, 1–8 (2012).
12. Lu, N. *et al.*  $\text{H}_3\text{PW}_{12}\text{O}_{40}/\text{TiO}_2$  catalyst-induced photodegradation of bisphenol A (BPA): kinetics, toxicity and degradation pathways. *Chemosphere* **91**, 1266–1272 (2013).
13. Xu, L. *et al.* Simulated sunlight photodegradation of aqueous phthalate esters catalyzed by the polyoxotungstate/titania nanocomposite. *J. Hazard. Mater.* **15**, 1070–1077 (2010).
14. Yurdakal, S., Tek, B. S., Degirmenci, C. & Palmisano, G. Selective photocatalytic oxidation of aromatic alcohols in solar-irradiated aqueous suspensions of Pt, Au, Pd and Ag loaded  $\text{TiO}_2$  catalysts. *Catal. Today* **281**, 53–59 (2017).
15. Sun, S., Wu, L., Png, C. E. & Bai, P. Nanoparticle loading effects on the broadband absorption for plasmonic-metal@semiconductor-microsphere photocatalyst. *Catal. Today* **278**, 312–318 (2016).
16. Zhao, Z. J. *et al.* Three-dimensional plasmonic Ag/ $\text{TiO}_2$  nanocomposite architectures on flexible substrates for visible-light photocatalytic activity. *Sci. Rep.* **7**, 8915 (2017).
17. Yen, Y. C., Chen, J. A., Ou, S., Chen, Y. S. & Lin, K. J. Plasmon-enhanced photocurrent using gold nanoparticles on a three-dimensional  $\text{TiO}_2$  nanowire-web electrode. *Sci. Rep.* **7**, 42524 (2017).
18. Gong, J. Y., Imbault, A. & Farnood, R. The promoting role of bismuth for the enhanced photocatalytic oxidation of lignin on Pt- $\text{TiO}_2$  under solar light illumination. *Appl. Catal. B: Environ.* **204**, 296–303 (2017).
19. Yun, E. T. *et al.* Visible-light-induced activation of periodate that mimics dye-sensitization of  $\text{TiO}_2$ : simultaneous decolorization of dyes and production of oxidizing radicals. *Appl. Catal. B: Environ.* **203**, 475–484 (2017).
20. Ossama, E., Peng, Z., Mamoru, F. & Tetsuro, M. Facile preparation of nitrogen and fluorine codoped  $\text{TiO}_2$  mesocrystal with visible light photocatalytic activity. *Appl. Catal. B: Environ.* **192**, 80–87 (2016).
21. Zalfani, M. *et al.*  $\text{BiVO}_4/3\text{DOM TiO}_2$  nanocomposites: effect of  $\text{BiVO}_4$  as highly efficient visible light sensitizer for highly improved visible light photocatalytic activity in the degradation of dye pollutants. *Appl. Catal. B: Environ.* **205**, 121–132 (2017).
22. Kale, M. J., Avanesian, T. & Christopher, P. Direct Photocatalysis by plasmonic nanostructures. *ACS Catal.* **4**, 116–128 (2017).
23. Liu, T. X. *et al.* A general method to diverse silver/mesoporous-metal-oxide nanocomposites with plasmon-enhanced photocatalytic activity. *Appl. Catal. B: Environ.* **165**, 378–388 (2015).
24. Hou, W., Liu, Z., Pavaskar, P., Hung, W. H. & Cronin, S. B. Plasmonic enhancement of photocatalytic decomposition of methyl orange under visible light. *J. Catal.* **277**, 149–153 (2011).
25. Cushing, S. K. *et al.* Photocatalytic activity enhanced by plasmonic resonant energy transfer from metal to semiconductor. *J. Am. Chem. Soc.* **134**, 15033–15041 (2012).
26. Devi, L. G. & Kavitha, R. A review on plasmonic metal- $\text{TiO}_2$  composite for generation, trapping, storing and dynamic vectorial transfer of photogenerated electrons across the Schottky junction in a photocatalytic system. *Appl. Surf. Sci.* **360**, 601–622 (2016).
27. Ghosh, S. K. & Pal, T. Interparticle coupling effect on the surface plasmon resonance of gold nanoparticles: from theory to applications. *Chem. Rev.* **107**, 4797–4862 (2007).
28. Brongersma, M. L., Halas, N. L. & Nordlander, P. Plasmon-induced hot carrier science and technology. *Nat. Nanotechnol.* **10**, 25–34 (2015).
29. Liu, Z. M. *et al.* Understanding the growth mechanisms of Ag nanoparticles controlled by plasmon-induced charge transfers in Ag- $\text{TiO}_2$  film. *J. Phys. Chem. C* **119**, 9496–9505 (2015).
30. Gao, H. Q. *et al.* Plasmon enhancement on photocatalytic hydrogen production over the Z-scheme photosynthetic heterojunction system. *Appl. Catal. B: Environ.* **210**, 297–305 (2017).
31. Li, H. R., He, Y. R., Liu, Z. Y., Jiang, B. C. & Huang, Y. M. Rapid synthesis of broadband Ag@ $\text{TiO}_2$  core-shell nanoparticles for solar energy conversion. *Sol. Energ. Mat. Sol. C.* **166**, 52–60 (2017).
32. Madhavi, V., Kondaiah, P., Shaik, H. & Rao, G. M. Phase dependent photocatalytic activity of Ag loaded  $\text{TiO}_2$  films under sun light. *Appl. Surf. Sci.* **364**, 732–739 (2016).
33. Yao, Y. C., Dai, X. R., Hu, X. Y., Huang, S. Z. & Jin, Z. Synthesis of Ag-decorated porous  $\text{TiO}_2$  nanowires through a sunlight induced reduction method and its enhanced photocatalytic activity. *Appl. Surf. Sci.* **387**, 469–476 (2016).
34. Sowmiya, M. & Senthilkumar, K. Dissociation of  $\text{N}_2\text{O}$  on anatase  $\text{TiO}_2$  (001) surface - The effect of oxygen vacancy and presence of Ag cluster. *Appl. Surf. Sci.* **389**, 1220–1232 (2016).
35. Liu, R., Wang, P., Wang, X. F., Yu, H. G. & Yu, J. G. UV- and Visible-light photocatalytic activity of simultaneously deposited and doped Ag/Ag(I)- $\text{TiO}_2$  photocatalyst. *J. Phy. Chem. C.* **116**, 17721–17728 (2012).
36. Feng, Y. M. *et al.* Honeycomb-like ZnO mesoporous nanowall arrays modified with Ag nanoparticles for highly efficient photocatalytic activity. *Sci. Rep.* **7**, 11622 (2017).
37. Wang, X. F., Li, T. Y., Rui, Y., Yu, H. G. & Yu, J. G. Highly efficient  $\text{TiO}_2$  single-crystal photocatalyst with spatially separated Ag and F<sup>-</sup> bi-cocatalysts: orientation transfer of photogenerated charges and their rapid interfacial reaction. *J. Mater. Chem. A.* **4**, 8682 (2016).
38. Raul, Q. C., Carlos, S. V., Darr, J. A. & Parkin, I. P. Critical influence of surface nitrogen species on the activity of N-doped  $\text{TiO}_2$  thin films during photodegradation of stearic acid under UV light irradiation. *Appl. Catal. B: Environ.* **160–161**, 582–588 (2014).
39. Huo, Y. N. *et al.* Ordered microporous  $\text{Bi}_2\text{O}_3/\text{TiO}_2$  film coated on a rotating disk with enhanced photocatalytic activity under visible irradiation. *Appl. Catal. B: Environ.* **148–149**, 550–556 (2014).
40. Noguchi, T. & Fujishima, A. Photocatalytic degradation of gaseous formaldehyde using  $\text{TiO}_2$  film. *Environ. Sci. Technol.* **32**, 3831–3833 (1998).
41. Kitano, M., Takeuchi, M., Matsuoka, M., Thomas, J. M. & Anpo, M. Photocatalytic water splitting using Pt-loaded visible light-responsive  $\text{TiO}_2$  film photocatalyst. *Catal. Today* **120**, 133–138 (2007).
42. Yang, Y., Guo, Y. H., Hu, C. W. & Wang, E. B. Lacunary Keggin-type polyoxometalates-based macroporous composite films: preparation and photocatalytic activity. *Appl. Catal. A: Gen.* **252**, 305–314 (2003).
43. Li, D. F., Guo, Y. H., Hu, C. W., Jiang, C. J. & Wang, E. B. Preparation, characterization and photocatalytic property of the  $\text{PW}_{11}\text{O}_{39}^{7-}/\text{TiO}_2$  composite film towards azo-dye degradation. *J. Mol. Catal. A: Chem.* **207**, 183–193 (2004).
44. Zhang, H. M. *et al.* Defect-mediated formation of Ag cluster-doped  $\text{TiO}_2$  nanoparticles for efficient photodegradation of pentachlorophenol. *Langmuir* **28**, 3938–3944 (2012).
45. Heng, H. M., Gan, Q., Meng, P. C. & Liu, X. The visible-light-driven type III heterojunction  $\text{H}_3\text{PW}_{12}\text{O}_{40}/\text{TiO}_2\text{-In}_2\text{S}_3$ : a photocatalysis composite with enhanced photocatalytic activity. *J. Alloy. Compd.* **696**, 51–59 (2017).
46. Li, C. Q., Sun, Z. M., Ma, R. X., Xue, Y. L. & Zheng, S. L. Fluorine doped anatase  $\text{TiO}_2$  with exposed reactive (001) facets supported on porous diatomite for enhanced visible-light photocatalytic activity. *Micropor. Mesopor. Mat.* **243**, 281–290 (2017).
47. Moulder, J. F., Stickle, W. F., Sobol, P. E. & Bomben, K. D. In: J. Chastain (Ed.), Handbook of X-ray photoelectron spectroscopy, Perkin-Elmer Corporation, USA, pp. 182 (1992).
48. Yu, J. G., Xiong, J. F., Cheng, B. & Liu, S. W. Fabrication and characterization of Ag- $\text{TiO}_2$  multiphase nanocomposite thin films with enhanced photocatalytic activity. *Appl. Catal. B: Environ.* **60**, 211–221 (2005).
49. Singh, J. *et al.* Atom beam sputtered Ag- $\text{TiO}_2$  plasmonic nanocomposite thin films for photocatalytic applications. *Appl. Surf. Sci.* **411**, 347–354 (2017).

50. Meng, F. K. *et al.* Photocatalytic generation of hydrogen with visible-light nitrogen-doped lanthanum titanium oxides. *Catal. Today* **199**, 48–52 (2013).
51. Kumar, M. K. *et al.* Field effects in plasmonic photocatalyst by precise SiO<sub>2</sub> thickness control using atomic layer deposition. *ACS Catal.* **1**, 300–308 (2011).
52. Chen, M. *et al.* Remarkable synergistic effect between {001} facets and surface F ions promoting hole migration on anatase TiO<sub>2</sub>. *Appl. Catal. B: Environ.* **207**, 397–403 (2017).
53. Liang, L. M., Zhou, G., Mi, J. & Wu, Z. Y. Fabrication of visible-light-driven one-dimensional anatase TiO<sub>2</sub>/Ag heterojunction plasmonic photocatalyst. *Catal. Commun.* **24**, 48–51 (2012).
54. He, X. L., Cai, Y. Y., Zhang, H. M. & Liang, C. H. Photocatalytic degradation of organic pollutants with Ag decorated free-standing TiO<sub>2</sub> nanotube arrays and interface electrochemical. *J. Mater. Chem.* **21**, 475–480 (2011).
55. Low, J. X., Yu, J. G., Jaroniec, M., Wageh, S. & Al-Ghamdi, A. A. Heterojunction Photocatalysts. *Adv. Mater.* **29**, 1601694 (2017).
56. Liang, H. J., Jia, Z. C., Zhang, H. C., Wang, X. B. & Wang, J. J. Photocatalysis oxidation activity regulation of Ag/TiO<sub>2</sub> composites evaluated by the selective oxidation of Rhodamine B. *Appl. Surf. Sci.* **422**, 1–10 (2017).
57. Zhao, X., Zhang, W. W., Peng, C. C., Liang, Y. J. & Wang, W. Z. Sensitive surface-enhanced Raman scattering of TiO<sub>2</sub>/Ag nanowires induced by photogenerated charge transfer. *J. Colloid Interf. Sci.* **507**, 370–377 (2017).
58. Jaafar, N. F. *et al.* Direct *in situ* activation of Ag<sup>0</sup> nanoparticles in synthesis of Ag/TiO<sub>2</sub> and its photoactivity. *Appl. Surf. Sci.* **338**, 75–84 (2015).
59. Almeida, M. F. D., Bellato, C. R. & Miranda, L. D. L. & Milagres, J. L. Preparation of calcined hydroxalite/TiO<sub>2</sub>-Ag composite and enhanced photocatalytic properties. *Ceram. Int.* **43**, 1843–1852 (2017).
60. Kuvarega, A. T., Krause, R. W. M. & Mamba, B. B. Nitrogen/Palladium-codoped TiO<sub>2</sub> for efficient visible light photocatalytic dye degradation. *J. Phys. Chem. C* **115**, 22110–22120 (2011).
61. Zhao, K. *et al.* Design of H<sub>3</sub>PW<sub>12</sub>O<sub>40</sub>/TiO<sub>2</sub> nano-photocatalyst for efficient photocatalysis under simulated sunlight irradiation. *Appl. Surf. Sci.* **285**, 616–624 (2013).
62. Li, G. *et al.* 3D flower-like β-MnO<sub>2</sub>/reduced graphene oxide nanocomposites for catalytic ozonation of dichloroacetic acid. *Sci. Rep.* **7**, 43643 (2017).
63. Press-Kristensen, K., Lindblom, E., Schmidt, J. E. & Henze, M. Examining the biodegradation of endocrine disrupting bisphenol A and nonylphenol in WWTPs. *Water Sci. Technol.* **57**, 1253–1256 (2008).
64. Pandiyan, T. O., Rivas, M. J., MartíNez, J. O., Amezcua, G. B. & MartíNez-Carrillo, M. A. Comparison of methods for the photochemical degradation of chlorophenols. *J. Photoch. Photobio. A: Chem.* **146**, 149–155 (2002).
65. Zhao, J. C., Chen, C. C. & Ma, W. H. Photocatalytic degradation of organic pollutants under visible light irradiation. *Top. Catal.* **35**, 269–278 (2005).
66. Pan, C. S. & Zhu, Y. F. New type of BiPO<sub>4</sub> oxy-acid salt photocatalyst with high photocatalytic activity on degradation of dye. *Environ. Sci. Technol.* **44**, 5570–5574 (2010).
67. Kormali, P., Troupis, A., Triantis, T., Hiskia, A. & Papaconstantinou, E. Photocatalysis by polyoxometallates and TiO<sub>2</sub>: a comparative study. *Catal. Today* **124**, 149–155 (2007).
68. Yang, Y. X. *et al.* Preparation and enhanced visible-light photocatalytic activity of silver deposited graphitic carbon nitride plasmonic photocatalyst. *Appl. Catal. B: Environ.* **142–143**, 828–837 (2013).
69. Bertelli, M. & Selli, E. Reaction paths and efficiency of photocatalysis on TiO<sub>2</sub> and of H<sub>2</sub>O<sub>2</sub> photolysis in the degradation of 2-chlorophenol. *J. Hazard. Mater.* **138**, 46–52 (2006).

## Acknowledgements

This work was financially supported by the National Natural Science Foundation of China (51408109; 51478097; 41702370), the Science and Technology Project of Jilin Province (20160520078JH; 20170520080JH), the Fundamental Research Funds for the Central Universities (2412015KJ026; 2412016KJ030).

## Author Contributions

N. Lu designed the research and wrote the paper; Y. Wang performed measurements and analyzed the data; S. Ning analyzed the data; W. Zhao performed measurements; M. Qian performed measurements; Y. Ma collected samples; J. Wang collected samples; L. Fan made figures; J. Guan wrote the paper; X. Yuan contributed to writing.

## Additional Information

**Supplementary information** accompanies this paper at <https://doi.org/10.1038/s41598-017-17221-4>.

**Competing Interests:** The authors declare that they have no competing interests.

**Publisher's note:** Springer Nature remains neutral with regard to jurisdictional claims in published maps and institutional affiliations.



**Open Access** This article is licensed under a Creative Commons Attribution 4.0 International License, which permits use, sharing, adaptation, distribution and reproduction in any medium or format, as long as you give appropriate credit to the original author(s) and the source, provide a link to the Creative Commons license, and indicate if changes were made. The images or other third party material in this article are included in the article's Creative Commons license, unless indicated otherwise in a credit line to the material. If material is not included in the article's Creative Commons license and your intended use is not permitted by statutory regulation or exceeds the permitted use, you will need to obtain permission directly from the copyright holder. To view a copy of this license, visit <http://creativecommons.org/licenses/by/4.0/>.

© The Author(s) 2017